




Mechanochemical synthesis, crystal structure and ion conduction in the $\text{Gd}_2\text{Hf}_{2-x}\text{Ti}_x\text{O}_7$ system

Nayeli M. Cepeda-Sánchez¹, José A. Díaz-Guillén², Mirosław Maczka³, Ulises Amador⁴, and Antonio F. Fuentes^{1,*} 

¹Cinvestav Unidad Saltillo, 25900 Ramos Arizpe, Coahuila, Mexico

²División de Estudios de Posgrado e Investigación, Instituto Tecnológico de Saltillo, 25280 Saltillo, Coahuila, Mexico

³Institute of Low Temperature and Structure Research, Polish Academy of Sciences, 50-950 Wrocław 2, Poland

⁴Departamento de Química y Bioquímica, Facultad de Farmacia, Universidad San Pablo-CEU, 28668 Boadilla del Monte, Madrid, Spain

Received: 3 February 2017

Accepted: 22 March 2017

Published online:

3 April 2017

© Springer Science+Business Media New York 2017

ABSTRACT

This work describes the mechanochemical synthesis, structural characterization and electrical properties of an interesting group of novel ionic conductors, with general formula $\text{Gd}_2(\text{Hf}_{2-x}\text{Ti}_x)_2\text{O}_7$. Different compositions in this system ($x = 0, 0.4, 0.8, 1.2, 1.6$ and 2) were obtained at room temperature, via a mechanochemical reaction between the corresponding elemental oxides, and characterized by using XRD, Raman spectroscopy and SEM. The XRD structural analysis by the Rietveld method revealed that all the Hf-containing compositions show a disordered fluorite-like structure instead of the expected pyrochlore-like atomic ordering, and the cation size mismatch criteria for pyrochlore stability. Increasing Ti content promotes a phase transformation to the pyrochlore structure with post-milling thermal treatments, which takes place in all samples on annealing at $1200\text{ }^\circ\text{C}$, except for $\text{Gd}_2\text{Hf}_2\text{O}_7$. These results were confirmed by Raman spectroscopy, which also suggests that the $x = 0.4$ sample has the highest degree of oxygen disorder in the system and that this disorder decreases with increasing Ti^{4+} content. Finally, all samples show the pyrochlore structure on firing at $1500\text{ }^\circ\text{C}$. Activation energies E_{dc} for oxygen migration were determined by using impedance spectroscopy and found to be within the $\sim 0.9\text{--}1.2\text{ eV}$ range, whereas conductivity σ_{dc} values at $700\text{ }^\circ\text{C}$ vary from 1.12×10^{-6} to $2.75 \times 10^{-4}\text{ S cm}^{-1}$, with decreasing conductivity as Ti^{4+} content increases.

Address correspondence to E-mail: fuentesaf@live.com

Introduction

Lanthanide hafnates $\text{Ln}_2\text{Hf}_2\text{O}_7$ adopting the pyrochlore and/or fluorite structure belong to a group of complex oxides, which have drawn considerable attention in recent years; in addition to high chemical and structural flexibility, they also show a rich variety of intriguing chemical and physical properties of fundamental and practical importance [1–4]. In particular, research interest in the ion conducting properties of this family of oxides dates back to the early 1980s, when high oxygen ion mobility at high temperatures was discovered in some $\text{Ln}_2\text{Zr}_2\text{O}_7$ compounds [5–7]. Typical oxygen ion conducting materials such as ZrO_2 or CeO_2 require doping with aliovalent cations (e.g., Ca^{2+} , Y^{3+} , Ln^{3+}) to create the anion vacancies that support conduction and are therefore *extrinsic* ionic conductors [8]. By contrast, anion vacancies are inherently present in $\text{Ln}_2\text{B}_2\text{O}_7$ oxides ($\text{Ln} = \text{Ln}^{3+}$; $\text{B} =$ tetravalent cation) and conduction does not require the incorporation of dopants; therefore, $\text{Ln}_2\text{B}_2\text{O}_7$ oxides are *intrinsic* oxygen ion conductors. Although many different $\text{Ln}_2\text{B}_2\text{O}_7$ systems ($\text{B} = \text{Sn}$, Ti , Zr) have been already synthesized and systematically analyzed [9–14], similar HfO_2 -based complex oxides remain relatively unexplored [15–21]. This contribution presents a study of the $\text{Gd}_2(\text{Hf}_{2-x}\text{Ti}_x)\text{O}_7$ system; to the best of our knowledge, this is the first time that the mechanochemical synthesis, structural characterization and electrical properties of this solid solution are analyzed. The chemistry of HfO_2 and ZrO_2 is very similar, and both form analogous complex oxides; however, the physical properties of their derivatives might be substantially different because Hf^{4+} and Zr^{4+} have similar ionic radii (R in sixfold coordination = 0.71 vs. 0.72 Å, respectively [22]) but very different electronic density (atomic numbers 72 vs. 40).

Because of the refractory nature of HfO_2 and Ln_2O_3 , preparing lanthanide hafnates by the traditional ceramic method requires lengthy firing cycles at very high temperatures (≥ 1500 °C) [18, 20]. By contrast, all samples analyzed in this work were obtained at room temperature, using a mechanochemical reaction. Mechanochemical methods have become very popular for the synthesis of a wide variety of materials [23, 24]; some of its advantages are the simplicity, the lack of solvents and the possibility of preparing large volumes of the target material using a cost-effective

method. Since reactants are processed under non-equilibrium conditions, uncommon and highly defective metastable phases are frequently obtained. Furthermore, additional processing (e.g., post-milling thermal treatments) offers the possibility of isolating fairly stable intermediate states, which are inaccessible for more conventional powder processing techniques.

From the crystallochemical point of view and depending on the $R_{\text{Ln}}/R_{\text{B}}$ size ratio, $\text{Ln}_2\text{B}_2\text{O}_7$ oxides will generally adopt either the anion-deficient fluorite structure ($R_{\text{Ln}}/R_{\text{B}} < 1.46$) or the pyrochlore structure ($R_{\text{Ln}}/R_{\text{B}} \geq 1.46$) [25]. The well-known ideal fluorite structure can be described as a face-centered cubic array of cations (S.G. = $Fm\bar{3}m$ (225); $Z = 4$), with anions placed at all the available tetrahedral interstices. The ideal pyrochlore structure is also isometric (S.G. = $Fd\bar{3}m$ (227); $Z = 8$) and might be considered as an ordered derivative of the anion-deficient fluorite structure, i.e., cations and anions are ordered each, in two symmetry-independent sites. Selecting the origin choice 2 of the space group 227, the larger cation (i.e., Ln^{3+}) is generally confined to the 16c Wyckoff position (0,0,0), coordinated by a distorted cuboctahedron of neighboring oxygen sites (two $\langle \text{Ln}-\text{O} \rangle$ bonds are significantly shorter than the rest). The smaller cation (B^{4+}) is placed at the 16d site (1/2,1/2,1/2), at the center of a trigonal antiprism, with all six $\langle \text{B}-\text{O} \rangle$ bonds of equal length. The anion substructure contains two tetrahedrally coordinated but independent oxygen ions located at the 48f ($x,1/8,1/8$) and 8a (1/8,1/8,1/8) Wyckoff sites. Therefore, pyrochlore oxides might be better represented as $\text{Ln}_2\text{B}_2\text{O}(1)_6\text{O}(2)$ ($\text{O}(1) = \text{O}_{48f}$; $\text{O}(2) = \text{O}_{8a}$). There is also an additional interstitial site in the unit cell, Wyckoff site 8b (3/8,3/8,3/8), easily accessible for anions, which is nominally vacant in ideal pyrochlore structures. As disorder increases ($R_{\text{Ln}}/R_{\text{B}} \approx 1.46$), this site becomes increasingly populated by O_{48f} and O_{8a} ions facilitating oxygen diffusion, and transforming pyrochlore oxides into fast ion conductors. According to calculations [26, 27], the energetically preferred pathway for oxide ion migration will consist of $\text{O}_{48f} \rightarrow \text{O}_{48f}$ sequential jumps, along the shortest edges of the BO_6 polyhedra. Increasing Ti content in the $\text{Gd}_2(\text{Hf}_{2-x}\text{Ti}_x)\text{O}_7$ system will increase the $R_{\text{Ln}}/R_{\text{B}}$ size ratio and thus the stability of the pyrochlore structure (i.e., the degree of structural order). The goal of this work is precisely to analyze

the effect of the Hf/Ti ratio, on the structural peculiarities and electrical properties of the title solid solution, on samples prepared by using mechanochemical methods.

Materials and methods

Different compositions in the $\text{Gd}_2(\text{Hf}_{2-x}\text{Ti}_x)\text{O}_7$ system ($x = 0, 0.4, 0.8, 1.2, 1.6$ and 2) were prepared at room temperature, by milling stoichiometric mixtures of the corresponding high purity ($\geq 99\%$) elemental oxides, *baddeleyite*-type HfO_2 , *anatase*- TiO_2 and $\text{C-Gd}_2\text{O}_3$. Milling was carried out in a Retsch PM400 planetary ball mill, using yttria partially stabilized zirconia (5 wt% Y_2O_3) containers (volume = 125 ml; sample size = 20 g) and grinding media (20 mm \varnothing ; balls-to-powder mass ratio = 10:1; rotation speed = 350 rpm). Phase evolution on milling was followed by using X-ray diffraction (XRD); the reaction time needed to achieve single-phase products was determined by examining at different intervals the XRD pattern of each reaction mixture, i.e., mechanically induced chemical reactions were considered completed when no traces of the starting oxides were evident by this technique. To analyze the relaxation process of mechanically induced defects, as-prepared samples were subjected to post-milling thermal treatments at 1200 and 1500 °C and analyzed as described below.

The structural and microstructural features of the title samples were obtained from precise diffraction data collected by using a Bruker D8 high-resolution X-ray powder diffractometer equipped with a Ge(111) primary monochromator ($\text{CuK}_{\alpha 1}$ radiation, $\lambda = 1.5406 \text{ \AA}$), and a LynxEye[®] rapid detector. The angular range, step size and counting times were adjusted to obtain good resolution (the step size should be at least 1/10th of the FWHMs) and statistics. The instrumental contribution to peak broadening was evaluated by using NIST LaB_6 standard reference material (SRM 660a; $\mu = 1138 \text{ cm}^{-1}$, linear absorption coefficient for $\text{CuK}_{\alpha 1}$ radiation). The structural refinements were performed by the Rietveld method, using the FullProf program [28]; since no secondary phases were detected by XRD, the chemical composition was included as constraint during the refinements. Therefore, the only free parameters for fluorite-like materials are the unit cell size and the isotropic thermal factors (Debye–Waller), whereas the relative

distribution of metal ions for pyrochlore-like phases was allowed to change between the two available sites while maintaining the nominal composition fixed. If needed crystallochemical criteria were used when assigning site occupancy preferences: smaller cations would preferentially occupy the sixfold oxygen-coordinated $16d$ site; correspondingly, larger ions would tend to sit at the eightfold coordinated $16c$ site. The samples microstructure was analyzed by using a phenomenological approach described in detail elsewhere [29–32]. As standard X-ray diffraction techniques are not adequate to study structural features related to light atoms, the oxygen array in our structural refinements is assumed to be ordered, as in the ideal pyrochlore structure, whereas 1/8th of the oxygen positions in fluorite-like phases were considered vacant at random.

The title samples were also characterized by Raman spectroscopy using a Horiba Scientific LabRAM HR Evolution NIR spectrometer, equipped with an Olympus BX41 confocal microscope, a solid-state blue excitation laser (473 nm) and a liquid N_2 cooled CCD detector. Raman spectroscopy is especially sensitive to anion disorder in $\text{Ln}_2\text{B}_2\text{O}_7$ pyrochlore-type oxides, since the spectra are entirely produced by the vibrations of the anion substructure, whereas the Ln and B cations reside in inversion centers ($16c$ and $16d$ sites symmetry is D_{3d}) and generate non-active Raman phonon modes. Powders were also examined by scanning electron microscopy (SEM) using a Philips XL30 ESEM microscope equipped with an EDAX Inc. energy-dispersive X-ray detector for microanalysis.

For the electrical characterization, as-prepared powders were uniaxially pressed (7 Tons cm^{-2}) into pellets (10 mm diameter and $\sim 1 \text{ mm}$ thickness) and sintered at 1500 °C for 12 h (heating/cooling rate = $5 \text{ }^\circ\text{C min}^{-1}$). The density of the sintered pellets was determined by the Archimedes' principle, using an Ohaus Discovery DV314C analytical balance ($\pm 0.1 \text{ mg}$), equipped with a density determination accessory (P/N 77402-00), and water as immersion medium. AC impedance measurements were carried out in air, as a function of frequency (100 Hz to 1 MHz) and temperature, using a Solartron 1260 frequency response analyzer. Electrodes for impedance spectroscopy were made by coating opposite faces of the pellets, with conductive Pt paste and firing in air at 800 °C to eliminate organic components and harden the Pt residue.

Results and discussion

Mechanochemical synthesis

Figure 1 shows the XRD patterns of a reaction mixture, ($1.6 \text{ HfO}_2 + 0.4 \text{ TiO}_2 + \text{Gd}_2\text{O}_3$), selected as representative of the series: as weighed (1a), and after different milling times (1b). To ease the discussion, the Miller indexes of the most intense reflections, characteristic of each starting chemical, have been labeled in Fig. 1a: baddeleyite-type $m\text{-HfO}_2$ (S.G. = $P2_1/c$ (14); JCPDS-ICDD PDF34-0104), *anatase*- TiO_2 (S.G. = $I4_1/amd$ (141); JCPDS-ICDD PDF21-1272) and C- Gd_2O_3 (S.G. = $Ia\bar{3}$ (206); JCPDS-ICDD PDF12-0797). Furthermore, the Bragg peaks of the three starting oxides are also shown at the bottom of the same figure. As observed in this figure, even milling for only 1 h produces important changes in the XRD pattern of the starting mixture. The usual effects of decreasing intensity and broadening of all diffraction peaks on milling because of a decreasing particle size, and increasing concentration of structural defects, are more pronounced for *anatase*- TiO_2 , and C- Gd_2O_3 , than for $m\text{-HfO}_2$, in agreement with the latter higher Moh's hardness. The characteristic reflections of the first two have disappeared almost completely, after milling for 1 h: the $m\text{-HfO}_2$ ($\bar{1}11$) and (111) lines at 28.36° and 31.69° (2θ), respectively, become the most intense of the whole pattern. In addition to these $m\text{-HfO}_2$ lines, the XRD pattern obtained after 6 h shows new reflections emerging at for example, ~ 30 and $\sim 60^\circ$ (2θ), suggesting that a mechanochemical

reaction is taking place. The intensity of these new reflections increases with milling time, and is the only ones observed after 20 h; at this point, the XRD pattern obtained resembles that characteristic of a fluorite-like material. Further milling (10 h) does not produce noticeable changes in the XRD pattern. Figure 1b also shows the Bragg peaks of $m\text{-HfO}_2$, and pyrochlore-type $\text{Gd}_2\text{Ti}_2\text{O}_7$ (JCPDS-ICDD PDF23-0259) and $\text{Gd}_2\text{Zr}_2\text{O}_7$ (JCPDS-ICDD PDF80-0469); the latter was selected because it is isostructural with $\text{Gd}_2\text{Hf}_2\text{O}_7$, and there is not a high-quality entry in the JCPDS-ICDD databank for pyrochlore-type $\text{Gd}_2\text{Hf}_2\text{O}_7$. The absence of additional reflections suggests that mechanical milling is a feasible route to obtain complex oxides in this system, alternative to the traditional solid-state reaction at high-temperature method. Therefore, the same procedure was applied to prepare the remaining samples analyzed in this work. To study the relaxation of mechanochemically induced defects with additional processing, different portions of the as-prepared powders were fired at high temperature and analyzed as described in the previous section.

Structural characterization by XRD and Raman spectroscopy

Figure 2 shows the graphical result of fitting the X-ray diffraction patterns of three different $\text{Gd}_2(\text{Hf}_{2-x}\text{Ti}_x)\text{O}_7$ samples: (a) $x = 0.4$ milled for 30 h, (b) $x = 0.8$, milled and fired 12 h at 1200°C and (c) $x = 1.2$, milled and annealed 12 h at 1500°C .

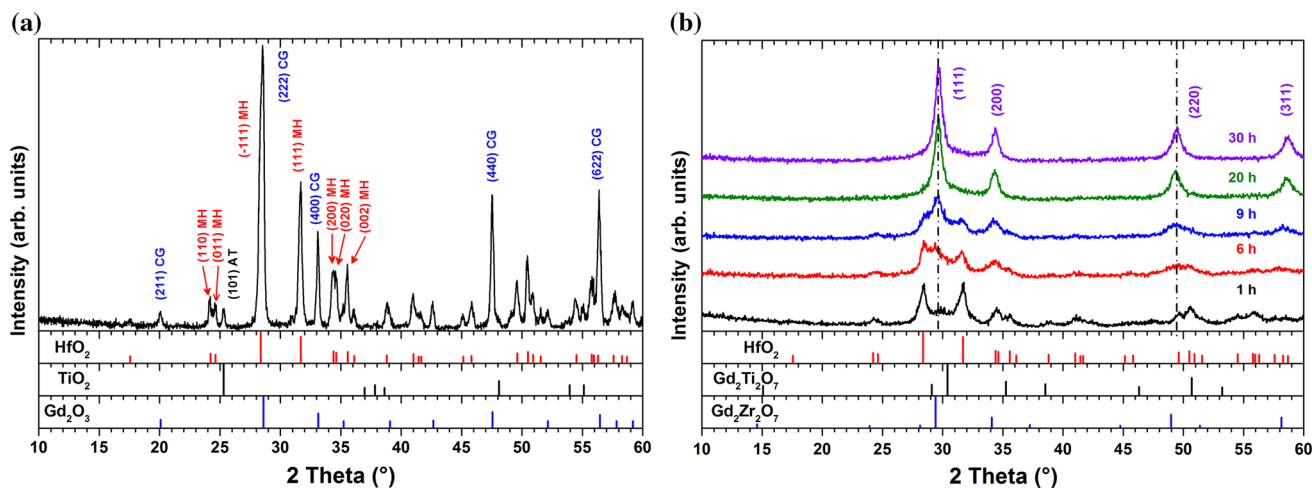


Figure 1 a XRD pattern of the starting $\text{Gd}_2\text{O}_3/\text{HfO}_2/\text{TiO}_2$ reaction mixture (molar ratio = 1:1.6:0.4) and b evolution of the same sample with milling time. Bragg peaks in a belong to the

three elemental oxides, whereas those in b belong to HfO_2 and pyrochlore type $\text{Gd}_2\text{Ti}_2\text{O}_7$ and $\text{Gd}_2\text{Zr}_2\text{O}_7$.

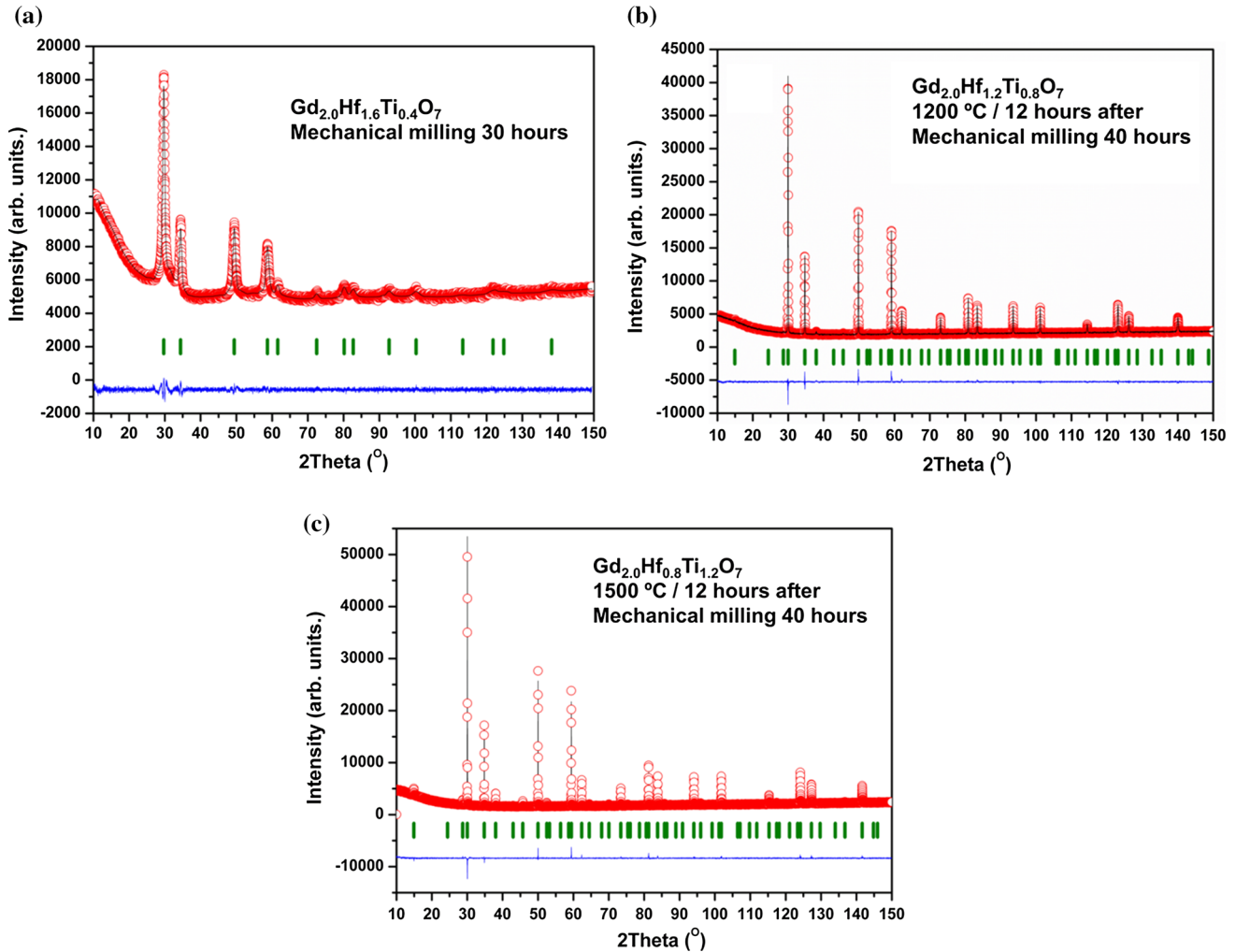


Figure 2 Graphical result of fitting the XRD patterns of three different $Gd_2(Hf_{2-x}Ti_x)O_7$ samples: **a** $x = 0.4$ milled for 30 h, **b** $x = 0.8$, milled and fired 12 h at 1200 °C and, **c** $x = 1.2$, milled and annealed 12 h at 1500 °C.

Table 1 Cations size mismatch in the $Gd_2Hf_{2-x}Ti_xO_7$ system. Ionic radii used for calculations are those given by Shannon [20]. An averaged R_B was calculated for mixed Hf/Ti compositions, taking into account the individual ionic radius and the fraction of each component cation

Composition	R_{Gd}/R_B
$Gd_2Hf_2O_7$	1.48
$Gd_2Hf_{1.6}Ti_{0.4}O_7$	1.53
$Gd_2Hf_{1.2}Ti_{0.8}O_7$	1.58
$Gd_2Hf_{0.8}Ti_{1.2}O_7$	1.63
$Gd_2Hf_{0.4}Ti_{1.6}O_7$	1.68
$Gd_2Ti_2O_7$	1.74

Table 1 shows the R_A/R_B size ratio for the title series, whereas the results of the structural refinement plus our samples microstructural features obtained from

the Langford plots [29–32] are collected in Tables 2, 3, 4.

The integral breadth (β) of diffraction lines in samples presenting complex microstructures as the title ones is related to “size” and “microstrain” effects. According to Langford [29, 30] and Halder and Wagner [32], both broadening effects can be separated by using the following equation [1]:

$$(\beta/d^*)^2 = \varepsilon^{-1}\beta/(d^*)^2 + (\eta/2)^2 \tag{1}$$

where ε gives the mean apparent domain size and η is a measure of the strain, related to the root mean square strain (e_{rms}) by $e_{rms} \sim \eta/5$. The graphical representation of equation [1] [$(\beta/d^*)^2$ vs. $\beta/(d^*)^2$] is the so-called Langford plot; the intercept gives the mean value of η , whereas the slope gives ε . Figure 3 shows such plots for the $Gd_2Hf_{0.4}Ti_{1.6}O_7$ sample

Table 2 Structural parameters of just-milled $\text{Gd}_2(\text{Hf}_{2-x}\text{Ti}_x)\text{O}_7$ powders, as obtained from their XRD patterns

Sample composition	$x = 0.4$	$x = 0.8$	$x = 1.2$	$x = 1.6$
a (Å)	5.2158 (4)	5.2056 (7)	5.1714 (4)	5.1500 (7)
R_B (%)	0.71	1.23	1.23	4.68
R_{wp} (%)	1.54	1.34	2.15	1.68
R_{exp} (%)	1.32	1.27	1.57	1.63
χ^2	1.36	1.11	1.52	1.07
$\langle D_{iso} \rangle$ (Å) ^a	71 (10)	61 (5)	56 (6)	74 (7)
e_{rms}^b	$6(3) \times 10^{-3}$	$3(3) \times 10^{-3}$	$10(3) \times 10^{-3}$	$14(8) \times 10^{-3}$

Powders obtained by mechanical milling (30 h). The structure is fluorite-like of $Fm\bar{3}m$ symmetry (S.G. #225). Gd^{3+} , Hf^{4+} and Ti^{4+} ions are randomly distributed at the $4a$ (0 0 0) sites, whereas oxygen atoms reside at the $8c$ ($\frac{1}{4}$ $\frac{1}{4}$ $\frac{1}{4}$) site. The respective occupations are those given by the chemical formula. Cell content is obtained as the site multiplicity times the occupancy; $Z = 4$

^a D_{iso} is the average domain diameter, assuming spherical shape

^b e_{rms} is the mean square strain in the structure

Table 3 Structural parameters of mechanochemically prepared $\text{Gd}_2(\text{Hf}_{2-x}\text{Ti}_x)\text{O}_7$ powders, after firing them at 1200 °C for 12 h as obtained from their XRD patterns

Sample composition	$x = 0^a$	$x = 0.4$	$x = 0.8$	$x = 1.2$	$x = 1.6$	$x = 2.0$
a (Å)	5.24511 (5)	10.42488 (2)	10.36981 (2)	10.32151 (1)	10.27171 (4)	10.20606 (4)
Gd/Ti/Hf at $16c$ (000)	–	1.61 (1)/–/0.39 (1)	1.402 (6)/0.40 (1)/0.202 (2)	1.637 (1)/0.126 (2)/0.237 (1)	1.896 (3)/0.104 (3)/–	1.869 (3)/0.131 (3)/–
Gd/Ti/Hf at $16d$ (1/21/21/2)	–	0.39 (1)/0.40/1.2 (1)	0.598 (6)/0.40 (1)/0.82 (6)	0.363 (1)/1.074 (2)/0.563 (1)	0.104 (3)/1.496 (3)/0.400	0.131 (3)/1.869 (3)/–
O (1) at $48f$ ($x1/81/8$)	–	1	1	1	1	1
x_{48f}	–	0.3957 (7)	0.4107 (6)	0.4104 (5)	0.4159 (4)	0.4258 (5)
O (2) at $8a$ (1/81/81/8)	–	1	1	1	1	1
R_B (%)	2.80	3.86	3.26	4.81	6.47	4.92
R_{wp} (%)	2.05	2.08	2.61	2.50	1.92	2.37
R_{exp} (%)	1.48	1.41	2.03	2.00	1.28	1.85
χ^2	1.92	2.16	1.66	1.56	2.81	1.65
$\langle D_{iso} \rangle$ (Å) ^b	565 (25)	–	FP 673 (9) 186 (5)	FP 1511 (73) 789 (30)	FP 1212 (18) 723 (10)	FP 2092 (120) 1223 (26)
e_{rms}^c	1.65 $(6) \times 10^{-3}$	–	FP $2.5(5) \times 10^{-4}$ $2.6(4) \times 10^{-3}$	FP $3.8(4) \times 10^{-4}$ $9(1) \times 10^{-4}$	FP 2.1 $(2) \times 10^{-4}$ $2(1) \times 10^{-4}$	FP 8.7 $(5) \times 10^{-5}$ $4.0(6) \times 10^{-4}$

^a For $x = 0$, the structure is fluorite-like of $Fm\bar{3}m$ symmetry (S.G. #225). Metal ions are randomly distributed at the $4a$ (000) sites, and oxygen atoms at $8c$ ($\frac{1}{4}$ $\frac{1}{4}$ $\frac{1}{4}$). The remaining samples present a pyrochlore-like structure of $Fd\bar{3}m$ symmetry (S.G. #227). The respective occupations are those given by the chemical formula. Cell content is obtained as the site multiplicity times the occupancy; $Z = 4$ for fluorite and 8 for pyrochlore

P and F denote pyrochlore and fluorite domains, respectively

^b D_{iso} is the average domain diameter, assuming spherical shape

^c e_{rms} is the mean square strain in the structure

Table 4 Structural parameters for mechanochemically prepared $\text{Gd}_2(\text{Hf}_{2-x}\text{Ti}_x)\text{O}_7$ powders, after firing at 1500 °C for 12 h as obtained from their XRD patterns

Sample composition	$x = 0^a$	$x = 0.4$	$x = 0.8$	$x = 1.2$	$x = 2.0$
a (Å)	10.49404 (2)	10.42064 (3)	10.36858 (1)	10.31717 (2)	10.2092 (6)
Gd/Ti/Hf at $16c$ (0 0 0)	1.41 (2)/–/0.59 (2)	1.76 (2)/–/0.24 (2)	1.680 (1)/0.080 (3)/0.249 (1)	1.767 (1)/0.040 (2)/0.194 (1)	1.961 (5)/0.084 (5)/–
Gd/Ti/Hf at $16d$ (1/2 1/2 1/2)	0.59 (2)/–/0.41 (2)	0.24 (2)/0.40/1.36 (2)	0.325 (1)/0.720 (3)/0.956 (1)	0.233 (1)/1.160 (2)/0.606 (1)	0.084 (5)/1.961 (5)/–
O(1) at $48f$ (x 1/8 1/8)	1	1	1	1	1
x_{48f}	0.4036 (5)	0.4085 (8)	0.4108 (6)	0.41457 (7)	0.4256 (5)
O(2) at $8a$ (1/8 1/8 1/8)	1	1	1	1	1
R_B (%)	5.57	5.67	4.42	5.04	4.49
R_{wp} (%)	2.50	3.27	2.68	2.83	2.38
R_{exp} (%)	1.24	1.60	2.04	2.14	1.86
χ^2	4.06	4.41	1.72	1.74	1.63
$\langle D_{iso} \rangle$ (Å) ^b	397 (13)	803 (14)	2911 (68)	Very large	Very large
e_{rms}^c	$6.1 (7) \times 10^{-5}$	$1.6 (9) \times 10^{-4}$	$1.3 (3) \times 10^{-4}$	No stress	No stress

^a All the samples present a pyrochlore-like structure with S.G. $Fd\bar{3}m$ (#227). The respective occupations are those given by the chemical formula. Cell content is obtained as the site multiplicity times the occupancy; $Z = 8$

corresponding, respectively, to just-milled powders (3a), and to powders milled and fired 12 h at 1200 °C (3b) and 1500 °C (3c). Worth mentioning is that poor-quality diffraction data obtained for our just-milled $\text{Gd}_2\text{Hf}_2\text{O}_7$ powders did not allow us to develop a valid and reliable structural model for this particular sample. As a superstructure of an anion-deficient fluorite-like atomic arrangement, the XRD pattern of a pyrochlore-type oxide contains a set of strong peaks characteristic of the fluorite-type substructure, plus an additional set of superstructure reflections [e.g., Miller indexes (111), (311) or (331) lines at $\sim 15^\circ$, $\sim 28^\circ$ and $\sim 38^\circ$ (2θ)] [33, 34]. The intensity of the latter depends on factors such as the degree of ordering, chemical composition (i.e., the difference in the average scattering factors of the constituent elements) and the distribution of oxygen vacancies. As shown in Table 1, both end members of the $\text{Gd}_2\text{H}_{2-x}\text{Ti}_x\text{O}_7$ system, $\text{Gd}_2\text{Hf}_2\text{O}_7$ and $\text{Gd}_2\text{Ti}_2\text{O}_7$, are isostructural and crystallize with the pyrochlore structure; therefore, according to the size ratio criteria for this structure' stability, the room temperature-stable form of any intermediate composition in the solid solution should be also a pyrochlore-like phase (see Table 1). However, the superstructure peaks are absent in the XRD patterns of our just-milled samples (see for instance Fig. 2a), except for $\text{Gd}_2\text{Ti}_2\text{O}_7$ [35], i.e., from the XRD point of view, long-range

pyrochlore-like atomic ordering is absent in these materials when obtained by using mechanochemical methods. Therefore, they are fluorite-like phases (Table 2) with all metal ions randomly distributed in the cation sublattice [Wyckoff $4a$ (0,0,0) site]. The lack of metal ordering is most likely a kinetic effect since mechanical milling often produces metastable phases. On the other hand, the only effect of the chemical composition is the expected contraction of the unit cell as the amount of Ti increases ($^{\text{VI}}R(\text{Ti}^{4+}) = 0.605$ Å, $^{\text{VI}}R(\text{Hf}^{4+}) = 0.71$ Å) [22]. Furthermore, both domain size and internal stress are apparently composition independent (Table 2).

Concerning the effect of post-milling thermal treatments at 1200 °C, the substitution of Hf^{4+} by Ti^{4+} enhances, as expected, the stability of the pyrochlore structure. Thus, the $\text{Gd}_2\text{Hf}_2\text{O}_7$ sample develops into a fluorite-type lattice, whereas increasing Ti^{4+} content induces the formation of pyrochlore-type (ordered) domains, coexisting with fluorite-like (disordered) ones (Table 3). Both domains grow with increasing Ti content although the ordered ones grow at a faster rate (almost an order of magnitude larger) than the disordered ones. The composition with $x = 0.4$ seems to be somehow "special" since it was not possible to determine, reliably, the size of the fluorite and pyrochlore domains. At first glance, the XRD pattern of this material appears to correspond to

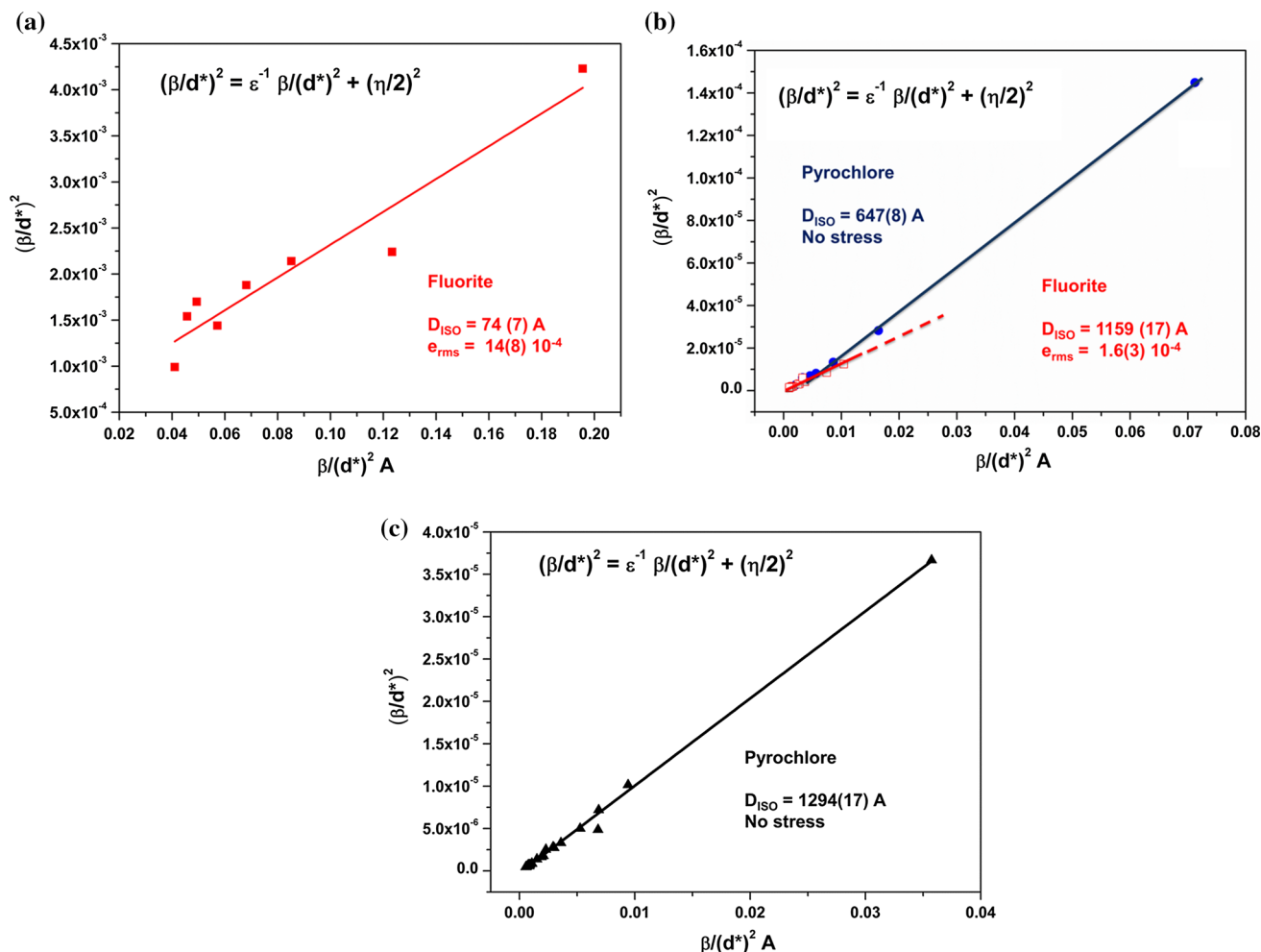


Figure 3 Langford plots for the $\text{Gd}_2\text{Hf}_{0.4}\text{Ti}_{1.6}\text{O}_7$ sample corresponding, respectively, to just-milled powders (a) and to powders milled and fired 12 h at 1200 °C (b) and 1500 °C (c).

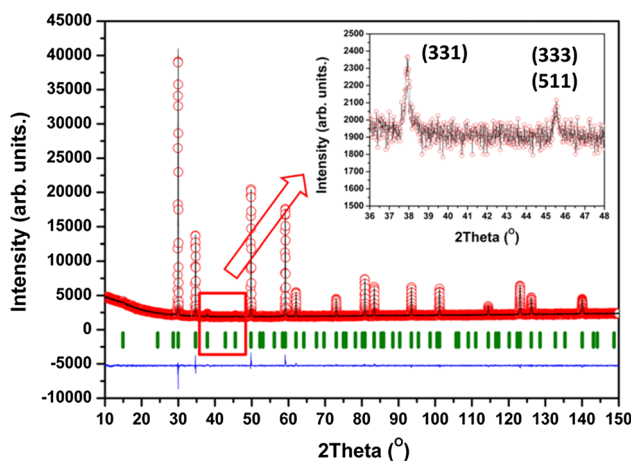


Figure 4 Graphical result of fitting the XRD pattern of the $\text{Gd}_2(\text{Hf}_{1.6}\text{Ti}_{0.4})\text{O}_7$ sample, after firing 12 h at 1200 °C. The *inset* shows a zoom of an area of this pattern, where some pyrochlore superstructure reflections can be observed.

a fluorite-like phase, since the only strong peaks observed are those of the basic unit (sub)cell, common to fluorite and pyrochlore structures. However, the diffraction peaks are rather broad, and the unit cell determined experimentally does not match that of a fluorite structure. A close inspection of the pattern reveals barely some very weak peaks corresponding to the pyrochlore superstructure (Fig. 4); probably, the similarity of scattering powers at both metal sites for this particular composition masks any possible cation ordering effect in the XRD pattern. Therefore, the only peaks clearly observed are those that belong to the fluorite substructure making almost impossible to evaluate any domain size effect on the diffraction peaks. As expected on the basis of crystalchemical considerations, small Ti^{4+} ions tend to occupy preferentially the BO_6 octahedral site displacing the larger Gd^{3+} and Hf^{4+} cations to the

16c-site. However, a significant amount of titanium ions are located at the larger 16c-sites, when $x > 0.4$. In summary, firing these mechanochemically prepared samples at 1200 °C induces cation ordering among the 16c- and 16d-sites, with each ion occupying likely a given position according to its size and crystallochemical properties. However, 1200 °C is not a sufficiently high temperature to reach complete ordering, and some anti-site defects still remain.

Finally, all samples present a pyrochlore-like structure after firing for 12 h at 1500 °C, and the atomic distribution is very close to that of the thermodynamic equilibrium. Indeed, based only on metal ions size, one would expect the large and eight-coordinated 16c site to be fully occupied by Gd^{3+} ions, whereas the smaller Ti^{4+} and Hf^{4+} ions would share the sixfold position (16d). As shown in Table 4, that is the general picture. However, some structural disorder remains even at this temperature. Generally speaking, small Ti ions tend to occupy the 16d-site, whereas the eight-coordinated positions are preferentially occupied by large Gd^{3+} ions. However, even for high “ x ” values (high Ti content), a limited but significant amount of Ti^{4+} ions are placed at the 16c-site; similarly, a non-negligible amount (*c.a.* 10%) of Gd^{3+} ions are located in the octahedral 16d-site, with a similar concentration of Hf^{4+} ions located at the 16c-site. According to a recent structural study on a similar system, $\text{Y}_2\text{Hf}_{2-x}\text{Ti}_x\text{O}_7$, a composition-induced pyrochlore-to-fluorite phase transition takes place when $x \approx 0.5$, in agreement with the cation size mismatch criteria [16]: $\text{Y}_2\text{Hf}_2\text{O}_7$ and $\text{Y}_2\text{Ti}_2\text{O}_7$ adopt, respectively, the fluorite and pyrochlore structures. However, no such phase transition is observed in the title Gd-containing system on samples fired at high temperature because as mentioned before, both end limits are pyrochlore-type structures.

Concerning these samples microstructure, it should be pointed out that temperature is very effective when releasing the internal structural stress, (Fig. 2c) with minor differences after firing at high temperature, due to material’s composition. By contrast, increasing Ti content seems to favor the growth of the pyrochlore domains, which as shown in Table 4 are considerably larger for the high-temperature fired samples.

As for Raman spectroscopy, selection rules state that fluorites should have only one Raman-active mode of F_{2g} symmetry, with the form of oxygen anions vibrating against the symmetry-fixed cations

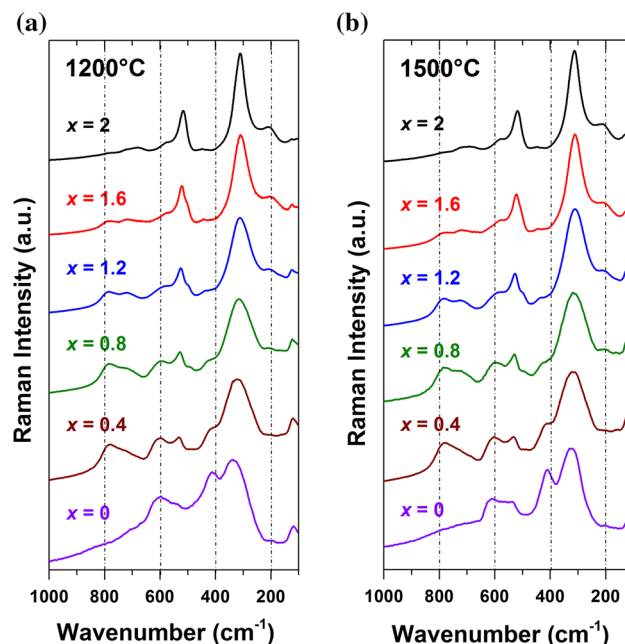


Figure 5 Raman spectra of the whole series of samples obtained by mechanical milling, after firing 12 h at 1200 (left) and 1500 °C (right).

[36]. A pyrochlore phase should have six Raman-active modes. Five of these modes ($A_{1g} + E_g + 3F_{2g}$) correspond to O_{48f} ions’ vibrations, and one mode (F_{2g}) to vibrations of the O_{8a} ions [35–37].

Raman spectra of the samples annealed at 1200 °C are presented in the left panel of Fig. 5. For $x = 0$, two strongest bands are observed at 337 and 412 cm^{-1} . By comparison with the Raman data reported for $\text{La}_2\text{Hf}_2\text{O}_7$ pyrochlore, these bands can be attributed to the $F_{2g} + E_g$ and F_{2g} modes, respectively [38]. Furthermore, the A_{1g} mode of $\text{La}_2\text{Hf}_2\text{O}_7$ can be located together with one F_{2g} mode at 514 cm^{-1} , and the last expected F_{2g} mode at 538 cm^{-1} [38]. However, Mandal et al. [39] have also suggested that the last expected F_{2g} mode for $\text{Dy}_2\text{Hf}_2\text{O}_7$ can be observed near 600 cm^{-1} . Our spectra show a weak band at 543 cm^{-1} that could be assigned to the A_{1g} mode and a relatively strong band at 602 cm^{-1} that can be most likely attributed to the F_{2g} mode. The fourth F_{2g} mode cannot be clearly seen, but the spectrum of the $x = 0.4$ sample shows the presence of a very weak band near 490 cm^{-1} that might be attributed to this mode.

Figure 5 shows that the observed bands for the $x = 0$ sample are very broad, much broader than previously reported [38] for pyrochlore-type $\text{La}_2\text{Hf}_2\text{O}_7$. Furthermore, the A_{1g} mode characteristic of a

pyrochlore structure is very weak. This behavior proves that this sample has a fluorite-type structure. Increasing concentration of Ti^{4+} ions leads to a shift of the 337, 543 and 602 cm^{-1} bands, to lower frequencies ($309, 515$ and 577 cm^{-1} for $x = 2$), whereas the opposite trend is observed for the 412 and 490 cm^{-1} bands (for $x = 2$, the former band shifts to 446 cm^{-1} and the latter merges with the 515 cm^{-1} band). Interestingly, the intensity of the A_{1g} mode strongly increases with increasing Ti^{4+} content. This band is known to be very sensitive to disorder, i.e., increasing structural disorder leads to strong broadening, and decreasing intensity of this band [38, 40]; the observed behavior indicates that doping with Ti^{4+} leads to the growth of the pyrochlore-like domains, in agreement with the X-ray diffraction data. The spectrum of the $x = 2$ sample is very similar to the Raman spectrum reported for $\text{Gd}_2\text{Ti}_2\text{O}_7$ single crystal [37], proving that this sample has a pyrochlore structure with small disorder.

It is worth noting that the $x = 0$ sample shows the presence of extra, very broad bands near 730 and 830 cm^{-1} . With increasing concentration of Ti^{4+} , the intensity of these bands strongly increases first for $x = 0.4$, and then decreases when $x > 0.4$. Such high-frequency bands are related to disorder-activated oxygen vibrations [41]. As discussed by Sanjuán et al. [41], appearance of such bands can be explained assuming partial occupation of the empty $8b$ site of the pyrochlore structure by oxygen ions and/or by exchanging $16d$ sites with gadolinium. According to the X-ray diffraction data, the highest concentration of Gd^{3+} ions at $16d$ sites is observed for the $x = 0.8$ sample whereas the $x = 0.4$ and $x = 1.2$ samples have comparable amount of Gd^{3+} at the $16d$ sites (Table 3). However, the high-frequency bands are the strongest for $x = 0.4$ and much weaker for $x = 1.2$.

These data show, therefore, that cationic disorder alone cannot explain the observed changes in intensity of the high-frequency bands and that oxygen disorder contributes significantly to this behavior. Therefore, our results suggest that the $x = 0.4$ sample has the highest degree of oxygen disorder and that this disorder decreases with increasing Ti^{4+} content.

Annealing of the $x = 0$ sample at higher temperature, i.e., $1500\text{ }^\circ\text{C}$, leads to moderate narrowing of Raman bands (see Fig. 5, right panel). This behavior indicates that increased annealing temperature promotes more ordered structures. The increased annealing temperature has, however, very weak effect on the Raman spectra measured for the other samples, suggesting weak changes of both cationic and anionic disorders.

Electrical properties

Figure 6 shows two representative examples of our samples microstructure, $\text{Gd}_2\text{Hf}_{0.8}\text{Ti}_{1.2}\text{O}_7$ (a) and $\text{Gd}_2\text{Hf}_{0.4}\text{Ti}_{1.6}\text{O}_7$ (b), after pressing and firing at $1500\text{ }^\circ\text{C}$. Table 5 shows the density of such sintered pellets, as determined by the Archimedes method together with that calculated from the XRD data, and the relative density (%). All samples showed a fairly dense microstructure, with increasing Ti content increasing also the grain size. Figure 7 shows some results of the electrical characterization carried out on the title samples: Fig. 7a presents the variation of the real part of the conductivity of the $\text{Gd}_2\text{Hf}_{1.6}\text{Ti}_{0.4}\text{O}_7$ material, as a function of frequency and temperature (log–log representation), and Fig. 7b shows a Nyquist plot for the same sample ($400\text{ }^\circ\text{C}$).

The conductivity behavior with frequency observed in Fig. 7a at low temperatures ($<500\text{ }^\circ\text{C}$) can be described by the mathematical expression:

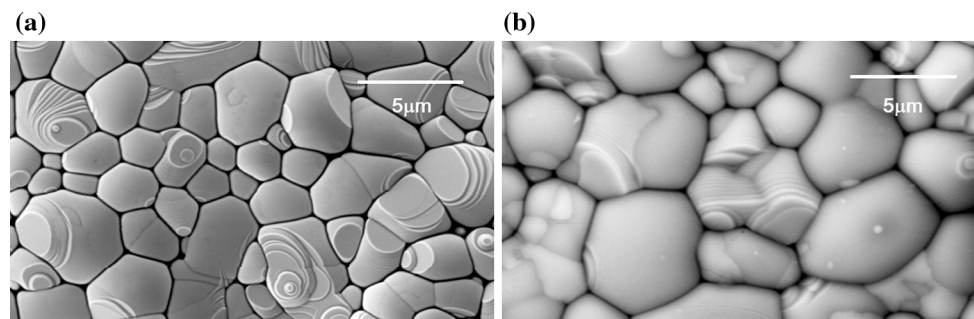


Figure 6 SEM micrographs showing the characteristic microstructure of these samples, after sintering 12 h at $1500\text{ }^\circ\text{C}$: $\text{Gd}_2\text{Hf}_{1.2}\text{Ti}_{0.8}\text{O}_7$ (left) and $\text{Gd}_2\text{Hf}_{0.4}\text{Ti}_{1.6}\text{O}_7$ (right).

Table 5 Theoretical (as determined from the XRD data) and experimental (Archimedes method) densities for pressed $Gd_2Hf_{2-x}Ti_xO_7$ powders, after sintering at 1500 °C

Composition	ρ_{XRD} (g cm ⁻³)	ρ (g cm ⁻³)	% Relative density
$Gd_2Hf_2O_7$	9.005	8.114	90.10
$Gd_2Hf_{1.6}Ti_{0.4}O_7$	8.584	7.123	82.98
$Gd_2Hf_{1.2}Ti_{0.8}O_7$	8.091	6.825	84.35
$Gd_2Hf_{0.8}Ti_{1.2}O_7$	7.581	6.729	88.76
$Gd_2Hf_{0.4}Ti_{1.6}O_7$	7.041	6.444	91.52
$Gd_2Ti_2O_7$	6.519	5.983	91.78

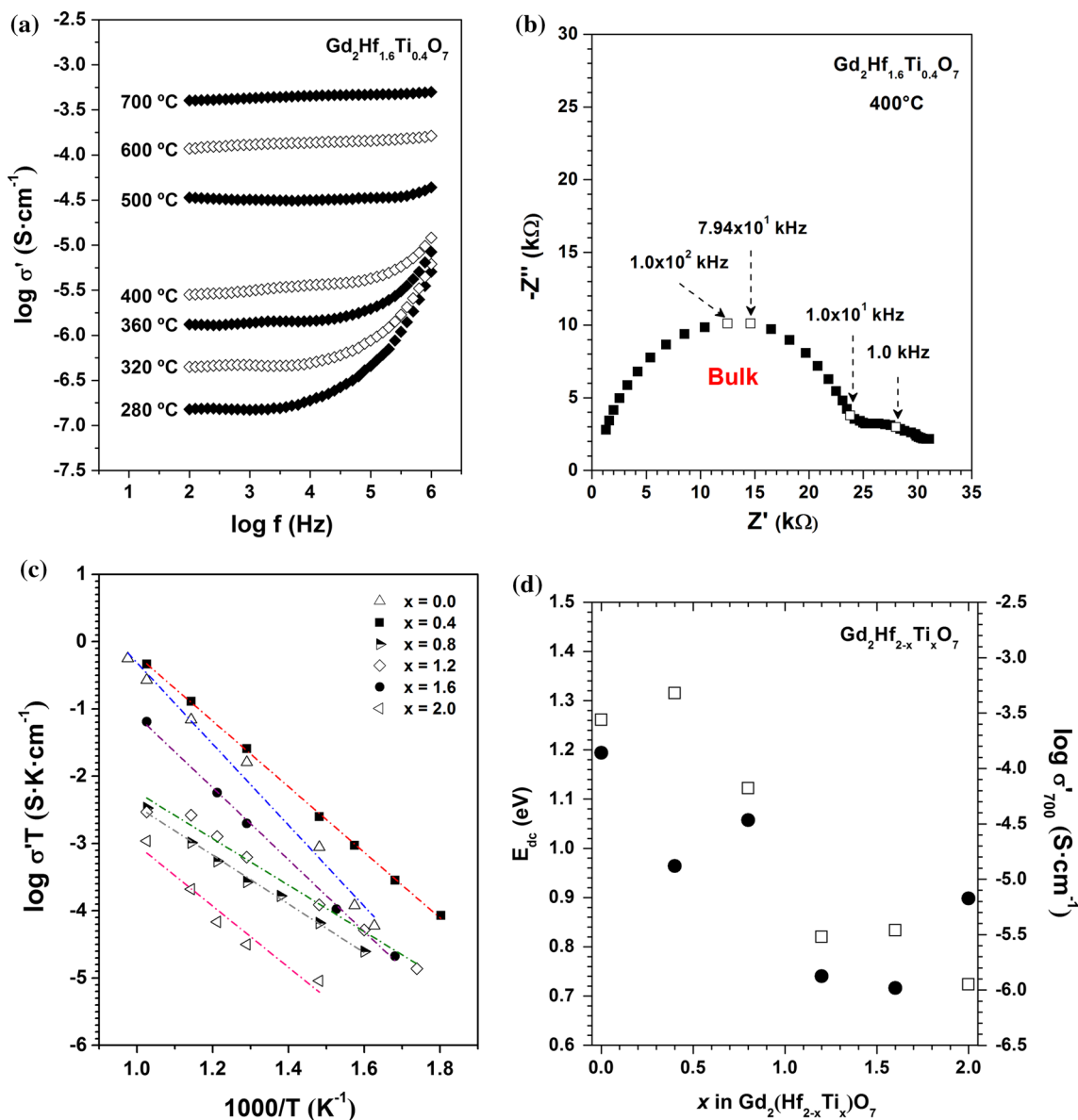


Figure 7 a Variation of the real part of the conductivity of the $Gd_2Hf_{1.6}Ti_{0.4}O_7$ material, as a function of frequency and temperature (log–log representation); b Nyquist plot of the same sample

at 400 °C; c Arrhenius-type plots for the conductivity in the series; d E_{dc} (solid circles) and σ' at 700 °C (empty squares), as a function of Ti content.

$$\sigma'(\omega) = \sigma_{dc} + A\omega^n, \quad (2)$$

where σ_{dc} is the dc conductivity, A is a temperature-dependent parameter and n is a fractional exponent, typically between 0.6 and 1. This expression is the signature of the so-called “Universal Dielectric Response” (UDR) [42], which is consistent with an (almost) constant conductivity value (σ_{dc}) at low frequencies, and a crossover at high frequencies, to a region of a power law-type dependence with frequency. This behavior has been associated with the existence of cooperative effects in the dynamics of mobile ions [43]. The crossover frequency between both regimes increases with increasing temperature and eventually above 500 °C shifts out of the experimental window. Two semicircles in the impedance plane are clearly observed in Fig. 7b. The one at low frequencies represents the grain boundary effects (capacitance values = 1.16×10^{-8} F cm⁻¹), whereas that at higher frequencies represents the bulk contribution (3.93×10^{-10} F cm⁻¹). Bulk dc conductivities at each temperature can be obtained either from the conductivity value at the frequency plateau in Fig. 7a or from the corresponding Nyquist plots, like the one shown in Fig. 7b. The temperature dependence of the bulk conductivity (σ_{dc}) in the title series was analyzed by using an Arrhenius-type expression of the form $(\sigma_{dc} \cdot T) = \sigma_0 \cdot \exp(-E_{dc}/k_B \cdot T)$, where σ_0 and E_{dc} are, respectively, the pre-exponential factor and the activation energy for oxygen ion migration. Figure 7c shows the corresponding graphical representation of the $(\sigma_{dc} \cdot T)$ dependence with the reciprocal of T , for all the samples analyzed. Dotted lines in this graph represent the experimental data least squares best fit to an Arrhenius-type law confirming that ionic diffusion in the samples is thermally activated; E_{dc} values can be easily calculated from the slope of such linear fits, and are shown in Table 6

Table 6 Calculated activation energies and conductivity at 700 °C, for the Gd₂Hf_{2-x}Ti_xO₇ system

Composition	σ_{dc} (S cm ⁻¹)	E_{dc} (eV)
Gd ₂ Hf ₂ O ₇	2.75×10^{-4}	1.194
Gd ₂ Hf _{1.6} Ti _{0.4} O ₇	4.78×10^{-4}	0.964
Gd ₂ Hf _{1.2} Ti _{0.8} O ₇	6.60×10^{-5}	1.057
Gd ₂ Hf _{0.8} Ti _{1.2} O ₇	3.01×10^{-6}	0.740
Gd ₂ Hf _{0.4} Ti _{1.6} O ₇	3.46×10^{-6}	0.716
Gd ₂ Ti ₂ O ₇	1.12×10^{-6}	0.898

together with the conductivity at 700 °C for the whole series. Figure 7d shows a graphical representation of these results as a function of the Ti⁴⁺ content. Calculated activation energies for the Hf-rich samples are in general ≈ 1 eV, similar to those reported in similar ion conducting systems [12], whereas E_{dc} for Ti-rich compositions decreases below 0.9 eV. Lower E_{dc} does not translate into higher conductivity and σ_{dc} decreases with increasing Ti⁴⁺ content. As structural disorder decreases with increasing Hf substitution, so does the number of mobile charge carriers and thus conductivity. However, the highest conductivity in the system corresponds to the Gd₂Hf_{1.6}Ti_{0.4}O₇ composition, instead of the one with the highest degree of disorder Gd₂Hf₂O₇. Decreasing number of mobile charge carriers with increasing structural ordering is apparently compensated in this particular composition by a lower activation energy for migration and thus conductivity increases in agreement with previous findings [12, 13].

Conclusions

We have shown that Hf-rich samples in the Gd₂(Hf_{2-x}Ti_x)₂O₇ system display fast to moderate ion conducting properties with activation energies on the order of ~ 1 eV and a peak in conductivity at 700 °C, for $x = 0.4$; typical σ_{dc} values measured for the oxygen ion conducting material par excellence, YSZ, are $\sim 10^{-2}$ S·cm⁻¹ at 800 °C and $\sim 10^{-1}$ S·cm⁻¹ at 1000 °C [44]. We have also shown that these otherwise highly refractory materials can be successfully obtained at room temperature via a mechanochemical reaction between the corresponding elemental oxides. According to the X-ray diffraction analysis, as-prepared powders crystallize with a fluorite-like structure, whereas post-milling thermal treatments at high temperature promote a phase transition to the thermodynamically stable, pyrochlore-like structure. As expected, the lattice parameter a in the system decreases with increasing Ti⁴⁺ content; the microstructural analysis revealed the presence of two types of domains: disordered fluorite-like domains coexisting in all samples, with ordered pyrochlore-like ones. Both types of domains grow with the level of substitution, but the pyrochlore-type grows at a faster rate (almost an order of magnitude larger) with increasing Ti content.

Acknowledgements

This work was financially supported by CONACYT (Grants CB2013-01-221701 and CB2011-01-166995). The authors acknowledge Prof. Maik Lang for providing the opportunity to carry out the Raman spectroscopy measurements at the University of Tennessee (Knoxville, TN), and Igor M. Gushev for his help when collecting the spectra.

Compliance with ethical standards

Conflict of interest The authors declare that they have no conflict of interest.

References

- [1] Gardner JS, Gingras MJP, Greedan JE (2010) Magnetic pyrochlore oxides. *Rev Mod Phys* 82:53–107
- [2] Ramirez AP, Hayashi A, Cava RJ, Siddharthan R, Sastry BS (1999) Zero-point entropy in “spin-ice”. *Nature* 399:333–335
- [3] Levi CG (2004) Emerging materials and processes for thermal barrier systems. *Curr Opin Solid State Mat Sci* 8:77–91
- [4] Sickafus KE, Minervini L, Grimes RW, Valdez JA, Ishimaru M, Li F, McClellan KJ, Hartmann T (2000) Radiation tolerance of complex oxides. *Science* 289:748–751
- [5] Van Dijk T, de Vries KJ, Burggraaf AJ (1980) Electrical conductivity of fluorite and pyrochlore $\text{Ln}_x\text{Zr}_{1-x}\text{O}_{2-x/2}$ ($\text{Ln} = \text{Gd}, \text{Nd}$) solid solutions. *Phys Stat Sol A* 58:115–125
- [6] Burggraaf AJ, van Dijk T, Verkerk MJ (1981) Structure and conductivity of pyrochlore and fluorite type solid solutions. *Solid State Ion* 5:519–522
- [7] Van Dijk MP, de Vries KJ, Burggraaf AJ (1985) Electrical conductivity and defect chemistry in the system $(\text{Tb}_x\text{Gd}_{1-x})_2\text{Zr}_2\text{O}_{7+y}$, ($0 \leq x \leq 1$; $0 \leq y \leq 0.25$). *Solid State Ion* 16:211–224
- [8] Subbarao EC, Maiti HS (1982) Solid electrolytes with oxygen ion conduction. *Solid State Ion* 11:317–338
- [9] Shlyakhtina AV, Fedtke P, Busch A, Kolbanev IV, Barfels T, Wienecke M, Sokolov AE, Ulianov VA, Trounov VA, Shcherbakova LG (2008) Effect of the Ca-doping on the electrical conductivity of oxide ion conductor $\text{Yb}_2\text{Ti}_2\text{O}_7$. *Solid State Ion* 179:1004–1008
- [10] Xia XL, Ouyang JH, Liu ZG (2010) Electrical properties of gadolinium-europium zirconate ceramics. *J Am Ceram Soc* 93:1074–1080
- [11] Porat O, Heremans C, Tuller HL (1997) Stability and mixed ionic electronic conduction in $\text{Gd}_2(\text{Ti}_{1-x}\text{Mo}_x)_2\text{O}_7$ under anodic conditions. *Solid State Ion* 94:75–83
- [12] Díaz-Guillén MR, Moreno KJ, Díaz-Guillén JA, Fuentes AF, Ngai KL, García-Barriocanal J, Santamaría J, León C (2008) Cation size effects in oxygen ion dynamics of highly disordered pyrochlore-type ionic conductors. *Phys Rev B* 78:104304
- [13] Díaz-Guillén JA, Fuentes AF, Díaz-Guillén MR, Almanza JM, Santamaría J, León C (2009) The effect of homovalent A-site substitutions on the ionic conductivity of pyrochlore-type $\text{Gd}_2\text{Zr}_2\text{O}_7$. *J Power Sources* 186:349–352
- [14] Shlyakhtina AV, Shcherbakova LG (2012) New solid electrolytes of the pyrochlore family. *Russ J Electrochem* 48:1–25
- [15] Kumar S, Gupta HC (2012) First principles study of dielectric and vibrational properties of pyrochlore hafnates. *Solid State Sci* 14:1405–1411
- [16] Kong L, Zhang Z, de los Reyes M, Karatchevtseva I, Lumpkin GR, Triani G, Aughterson RD (2015) Soft chemical synthesis and structural characterization of $\text{Y}_2\text{Hf}_x\text{Ti}_{2-x}\text{O}_7$. *Ceram Inter* 41:5309–5317
- [17] Anand VK, Bera AK, Xu J, Herrmannsdörfer T, Ritter C, Lake B (2015) Observation of long-range magnetic ordering in pyrohafnate $\text{Nd}_2\text{Hf}_2\text{O}_7$: a neutron diffraction study. *Phys Rev B* 92:184418
- [18] Blanchard PER, Liu S, Kennedy BJ, Ling CD (2013) Investigating the local structure of lanthanoid hafnates $\text{Ln}_2\text{Hf}_2\text{O}_7$ via diffraction and spectroscopy. *J Phys Chem C* 117:2266–2273
- [19] Shlyakhtina AV, Shcherbakova LG (2011) Polymorphism and high-temperature conductivity of $\text{Ln}_2\text{M}_2\text{O}_7$ ($\text{Ln} = \text{Sm}–\text{Lu}$; $\text{M} = \text{Ti}, \text{Zr}, \text{Hf}$) pyrochlores. *Solid State Ion* 192:200–204
- [20] Brixner LH (1984) Structural and luminescent properties of the $\text{Ln}_2\text{Hf}_2\text{O}_7$ -type rare earth hafnates. *Mat Res Bull* 19:143–149
- [21] Shlyakhtina AV, Knotko AV, Boguslavskii MV, Stefanovich SY, Kolbanev IV, Larina LL, Shcherbakova LG (2007) Effect of non-stoichiometry and synthesis temperature on the structure and conductivity of $\text{Ln}_{(2+x)}\text{M}_{(2-x)}\text{O}_{(7-x/2)}$ ($\text{Ln} = \text{Sm}–\text{Gd}$; $\text{M} = \text{Zr}, \text{Hf}$, $x = 0–0.286$). *Solid State Ion* 178:59–66
- [22] Shannon R (1976) Revised effective ionic radii and systematic studies of interatomic distances in halides and chalcogenides. *Acta Cryst* A32:751–767
- [23] Zyryanov VV (2008) Mechanochemical synthesis of complex oxides. *Russ Chem Rev* 77:105–135
- [24] Fuentes AF, Takacs L (2013) Preparation of multicomponent oxides by mechanochemical methods. *J Mater Sci* 48:598–611. doi:10.1007/s10853-012-6909-x
- [25] Subramanian MA, Aravamudan G, Subba Rao GV (1985) Oxide pyrochlores—a review. *Prog Solid State Chem* 15:55–143.

- [26] Van Dijk MP, Burggraaf AJ, Cormack AN, Catlow CRA (1985) Defect structures and migration mechanisms in oxide pyrochlores. *Solid State Ion* 17:159–167
- [27] Wilde PJ, Catlow CRA (1998) Defects and diffusion in pyrochlore structured oxides. *Solid State Ion* 112:173–183
- [28] Rodríguez-Carvajal J (1993) Recent advances in magnetic structure determination by neutron powder diffraction, *Phys B* 19:55–69; See also a report in CPD of IUCr, Newsletter 2001, 26, 12; available at <http://www.iucr.org/iucr-top/comm/cpd/Newsletters>. The program and manual can be found at <http://www-llb.cea.fr/fullweb/powder.htm>
- [29] Langford JI (1992) The use of the Voigt function in determining microstructural properties from diffraction data by means of pattern decomposition. In: Prince E, Stalick JK (eds) *Proceedings of the international conference "Accuracy in Powder Diffraction II"*. NIST Special Publication 846 Gaithersburg, MD, USA, pp 110–126
- [30] Langford JI (1999) Use of pattern decomposition or simulation to study microstructure: theoretical considerations. In: Snyder RL, Fiala J, Bunge HJ (eds) *Defect and microstructure analysis by diffraction*, IUCr Monographs on Crystallography 10. Oxford University Press, Oxford, pp 59–81
- [31] Louër D (1999) Use of pattern decomposition to study microstructure: practical aspects and applications. In: Snyder RL, Fiala J, Bunge HJ (eds) *Defect and microstructure analysis by diffraction*, IUCr Monographs on Crystallography 10. Oxford University Press, Oxford, pp 671–697
- [32] Halder NC, Wagner CNJ (1966) Analysis of the broadening of powder pattern peaks using variance, integral breadth, and Fourier coefficients on the line profile. *Adv X-Ray Anal* 9:91–102
- [33] Heremans C, Wuensch BJ, Stalick JK, Prince E (1995) Fast-ion conducting $Y_2(Zr_yTi_{1-y})_2O_7$ pyrochlores: neutron Rietveld analysis of disorder induced by Zr substitution. *J Solid State Chem* 117:108–121
- [34] Wuensch BJ, Eberman KW, Heremans C, Ku EM, Onnerud P, Yeo EME, Haile SM, Stalick JK, Jorgensen JD (2000) Connection between oxygen-ion conductivity of pyrochlore fuel-cell materials and structural change with composition and temperature. *Solid State Ion* 129:111–133
- [35] Fuentes AF, Boulahya K, Maczka M, Hanuza J, Amador U (2005) Synthesis of disordered pyrochlores, $A_2Ti_2O_7$ ($A = Y, Gd$ and Dy), by mechanical milling of constituent oxides. *Solid State Sci* 7:343–353
- [36] Moreno KJ, Fuentes AF, Maczka M, Hanuza J, Amador U, Santamaria J, Leon C (2007) Influence of thermally induced oxygen order on mobile ion dynamics in $Gd_2(Ti_{0.65}Zr_{0.35})_2O_7$. *Phys Rev B* 75:184303
- [37] Maczka M, Hanuza J, Hermanowicz K, Fuentes AF, Matsuhira K, Hiroi ZJ (2008) Temperature-dependent Raman scattering studies of the geometrically frustrated $Dy_2Ti_2O_7$, $Gd_2Ti_2O_7$ and $Er_2Ti_2O_7$. *J Raman Spectrosc* 39:537–544
- [38] Garg N, Pandey KK, Murli C, Shanavas KV, Mandal BP, Tyagi AK, Sharma SM (2008) Decomposition of lanthanum hafnate at high pressures. *Phys Rev B* 77:214105
- [39] Mandal BP, Garg N, Sharma SM, Tyagi AK (2006) Preparation, XRD and Raman spectroscopic studies on new compounds $RE_2Hf_2O_7$ ($RE = Dy, Ho, Er, Tm, Lu, Y$): pyrochlores or defect fluorite? *J Solid State Chem* 179:1990–1994
- [40] Glerup M, Nielsen OF, Poulsen FW (2001) The structural transformation from the pyrochlore structure, $A_2B_2O_7$, to the fluorite structure, AO_2 , studied by Raman spectroscopy and defect chemistry modeling. *J Solid State Chem* 160:25–32
- [41] Sanjuán ML, Guglieri C, Diaz-Moreno S, Aquilanti G, Fuentes AF, Olivi L, Chaboy J (2011) Raman and x-ray absorption spectroscopy of the phase evolution induced by mechanical milling and thermal treatments in $R_2Ti_2O_7$ pyrochlores. *Phys Rev B* 84:104207
- [42] Jonscher AK (1984) *Dielectric relaxation in solids*. Chelsea Dielectric Press, London
- [43] Moreno KJ, Fuentes AF, Amador U, Santamaria J, León C (2007) Influence of structural disorder on the dynamics of mobile oxygen ions in $Dy_2(Ti_{1-y}Zr_y)_2O_7$. *J Non-Cryst Solids* 353:3947–3955
- [44] Aguadero A, Fawcett L, Taub S, Woolley R, Wu K-T, Xu N, Kilner JA, Skinner SJ (2012) Materials development for intermediate-temperature solid oxide electrochemical devices. *J Mater Sci* 47:3925–3938. doi:10.1007/s10853-011-6213-1